

# Mapping hierarchical and heterogeneous micromechanics of a transformative high entropy alloy by nanoindentation and machine learning augmented clustering

Abhijeet Dhal <sup>a,b</sup>, Ravi Sankar Haridas <sup>b,c</sup>, Priyanka Agrawal <sup>a,b</sup>, Sanya Gupta <sup>a,b</sup>, Rajiv S. Mishra <sup>a,b,\*</sup>

<sup>a</sup> Department of Materials Science and Engineering, University of North Texas, Denton, TX 76201, USA

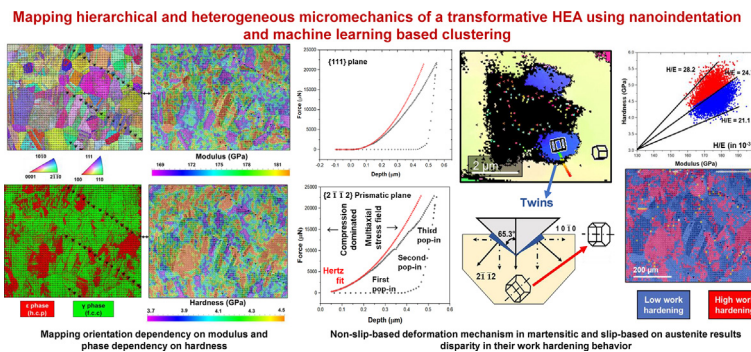
<sup>b</sup> Advanced Materials and Manufacturing Processes Institute, University of North Texas, Denton, TX 76201, USA

<sup>c</sup> Department of Mechanical Engineering, University of North Texas, Denton, TX 76201, USA

## HIGHLIGHTS

- Deformation in f.c.c. austenitic grains is slip-dominated and demonstrates orientation dependent incipient plasticity and phase transformation.
- Strong dependency of phase, crystal orientation, and interfacial constraints on the nanoindentation response was observed.
- A disproportionately high hardness is observed in martensite-rich area due to hierarchical activation various micromechanisms.
- Creation of coherent twin boundaries and dislocation activities in the twinned interfaces occurs during nanoindentation in martensitic regions.

## GRAPHICAL ABSTRACT



## ARTICLE INFO

### Article history:

Received 23 January 2023

Revised 8 April 2023

Accepted 22 April 2023

Available online 26 April 2023

### Keywords:

High entropy alloys  
Nanoindentation  
Machine learning  
Incipient plasticity  
Twinning  
Transformation-induced plasticity

## ABSTRACT

Conventional macromechanical tests provide limited insights into complex hierarchical deformation behavior of a transformative high entropy alloy (HEA). In this work, a high throughput microstructure-micromechanical correlative study is presented by combining high-resolution nanoindentation, site-specific microscopy, and Gaussian mixture model (GMM) clustering. The investigated HEA has a heterogenous microstructure consisting of austenite and martensite phases. Comparison of elastoplastic and microstructural maps illustrate dependency of phase, crystal orientation, and interfacial constraints on the micromechanical response. The disproportionately high hardness found in martensite-rich area is attributed to its higher lattice stability to shear, creation of coherent twin boundaries, and copious dislocation activities in the twin interfaces formed in martensite phase during nanoindentation. The hierarchy in twinning behavior depends on the relative direction of loading with the c-axis of h.c.p. martensitic phase. Deformation in f.c.c. austenitic grains is slip-dominated and demonstrates orientation dependency during incipient plasticity and phase transformation. GMM based classification of hardness to modulus ratio intuitively correlates work-hardening with phase distribution due to the distinctive deformation micromechanical responses of austenite and martensite phases.

© 2023 The Author(s). Published by Elsevier Ltd. This is an open access article under the CC BY-NC-ND license (<http://creativecommons.org/licenses/by-nc-nd/4.0/>).

\* Corresponding author at: Department of Materials Science and Engineering, University of North Texas, Denton, TX 76201, USA.

E-mail address: [rajiv.mishra@unt.edu](mailto:rajiv.mishra@unt.edu) (R.S. Mishra).

## 1. Introduction

The complex hierarchy in deformation mechanisms of transformative high entropy alloys (HEA) have caught considerable research attention in the recent few years [1]. The plastic deformation in these alloys is instigated by the dissociation of full dislocation into Shockley partials in austenitic phase ( $\gamma$ -f.c.c.). The slip activities of these partials define the primary deformation mechanism in the  $\gamma$ -f.c.c. phase. Non-slip-based micromechanics like twinning in  $\gamma$ -f.c.c., martensitic transformation ( $\gamma \rightarrow \epsilon$ ), and twinning in  $\epsilon$ -h.c.p. get hierarchically activated. Transformation-induced plasticity (TRIP) plays a pivotal role in the overall deformation and work hardening of these HEA [2]. Slip in the  $\gamma$ -f.c.c. onsets via planar dislocation glide of  $\frac{1}{2}[110]$  dislocations along {111} crystal direction [3]. Depending on the interaction between a pair of leading and trailing partials, deformation twin/martensite embryos are formed [4]. These embryos are formed by dissociation of  $\frac{1}{2}[110]$  full dislocations into  $\frac{1}{6}[112]$  partials on the {111} plane [5]. Depending on local stacking fault energy (SFE) within the microstructure, the embryos mature into either martensite or twins [6]. Dislocation activities in the martensitic  $\epsilon$ -h.c.p. phase are restricted to  $< c+a >$  and  $< a >$  slip which do not satisfy Taylor's five independent slip system criterion for homogenous deformation [7]. Therefore, twin induced plasticity (TWIP) dominates over slip and the relaxed twin interfaces provide coherent sites for additional dislocation activities due to their lower interfacial energy [8]. Further deformation leads to the intertwining of the martensitic bands, increasing activation sites for more dislocation activities. Densification of the martensite and twin networks continuously reduces the dislocation mean path and enhances the material's work-hardening capability [9].

To understand the complex heterogeneity and hierarchy in the deformation mechanisms, interrupted mechanical testing and microstructural analysis were performed on these HEAs [10]. However, the linkages between microstructure and mechanisms were established only at specific deformation strains. *In-situ* neutron/synchrotron tensile tests were performed to determine deformation mechanisms at broader range of strain [3,11,12]. However, the length-scale limitation of macro-mechanical tests prevented deeper microstructural-micromechanical understanding. Furthermore, these tests captured the cooperative deformation mechanisms of the entire microstructure and do not delineate the independent effect of phase and grain orientation. Nanomechanical testing such as nano-pillar compression, nanoscale tension and nanoindentation can complement micro/macromechanical tests to bridge this length scale gap and have recently gained popularity in determining local mechanical properties of HEAs [13–18]. The general drawback of nanomechanical tests is their location specificity and lack of statistical significance required to fully comprehend the HEA's complex mechanical response. Furthermore, large datasets are needed to explain the wide variation in micromechanisms due to inherent microstructural (such as phases, grain boundary, crystal orientation etc. [19]) dependency/anisotropy. Other factors such as surface roughness, process induced mechanical heterogeneity are co-contributors to the scatter in nanoscale mechanical responses [20]. However, nano-pillar compression and nanoscale tensile tests require time consuming sample preparation method using focused ion beam milling, which significantly increases the overall time required to test for large dataset.

High-resolution nanoindentation mapping using large number of indents is a quick, statistically robust, and high-throughput tool for microstructure-micromechanical correlation. It has been recently implemented to investigate the mechanical heterogeneity in additively manufactured alloys and graded/composite materials [21–25]. The use of high-resolution nanoindentation technique to

understand the complex deformation behavior of HEA has been limited. Tong *et al.* [26] determined the relative contribution of various phases with the hardness and modulus maps of CoCrNiMo HEA. Muskeri *et al.* [27] mapped the hardness distribution on ballistic impacted  $\text{Al}_{0.3}\text{CoCrFeNi}$  HEA. However, both these works did not explore the hierarchical multimechanical deformation route of transformative HEA, and there remains a wide scope to explore nanoindentation as an efficient tool to establish a strong microstructure-micromechanical relationship in transformative HEAs. Large dataset from nanoindentation mapping can be augmented with machine learning based clustering techniques such as  $k$ -cluster and Gaussian modelling to enhance these correlative analysis [28–32]. Furthermore, by using different tip geometries deformation pathway can be altered and the distinctive mechanical response can be studied during nanoindentation. For example, using Berkovich and cube-corner tips, a complex multiaxial stress field is exerted, and using spherical tip relatively simple compression dominated stress field is applied on the material [33]. Such an integrated approach is essential to advance alloy and process design paradigm of transformative HEA. In this view, this work a novel machine learning augmented high-throughput micromechanical study is used to obtain insight into the complex deformation behavior of a transformative HEA. The present investigation involves high resolution mapping using Berkovich tip and incipient plasticity study using a spheroc-conical tip of  $5\text{ }\mu\text{m}$  radius. Microstructural correlative study using site-specific electron microscopes is performed, and dependency of phase, crystal orientation, and interfacial constraints on the micromechanical response is investigated.

## 2. Methods and materials

Metastable transformative HEA with a chemical composition of  $\text{Fe}_{38.5}\text{Mn}_{20}\text{Co}_{20}\text{Cr}_{15}\text{Si}_5\text{Cu}_{1.5}$  (at.%) was supplied as 3 mm rolled sheets by Sophisticated Alloys Ltd. A coupon was cut out from the sheet and annealed at  $800\text{ }^\circ\text{C}$  for 30 min, followed by air cooling. This heat-treatment strategy [34] of holding in the lower end of austenitic temperature for a short period of time is expected to effectively relieve significant rolling strain while retaining the dual-phase heterogenous microstructural configuration.

Nanoindentation mapping was performed using FemtoTools FM-NMT04 nanoindenter equipped with Berkovich tip. Although, the exact tip radius of the Berkovich indenter is difficult to measure accurately [35], it is rated to be less than 50 nm by the instrument maker. For fundamental nanomechanical study, a spheroc-conical indenter with a known tip radius of  $5\text{ }\mu\text{m}$  was used. The test sample was polished to mitigate surface roughness errors. For polishing, a series of superfine emery papers followed by vibratory polishing using  $0.02\text{ }\mu\text{m}$  colloidal silica suspension is used. Before testing, tip area calibration was done using fused silica standard. Displacement controlled test was performed, in which the indentation displacement occurred in two stages: (i) nano-positioner actuates until a fixed load of  $50\text{ }\mu\text{N}$  is achieved under the tip, and (ii) piezo-actuator containing the Berkovich/spheroc-conical tip displaces to a constant depth of 500 nm. This approach enables local plastic deformation to occur at constant preload. For both mapping and nanomechanical investigation, a consistent loading rate of  $0.25\text{ }\mu\text{m/s}$ , and unloading rate of  $0.5\text{ }\mu\text{m/s}$  was utilized. During nanoindentation mapping using Berkovich indenter, a grid consisting of 10,000 indents was programmed for high statistical robustness of the mapped dataset. The inter-indent spacing was set as  $5\text{ }\mu\text{m}$  (i.e. 10 times of the indentation depth) to avoid overlap with plastic region of neighboring indents [28,36]. The instrument employed continuous stiffness measurement (CSM) to obtain continuous depth-dependent elastic-plastic response

during the loading stage. Oliver-Pharr's method was used to determine the hardness and modulus corresponding to each indentation [37]. After the completion of nanoindentation mapping, a few deeper indents were added on the right side of the grid. These indents were used as fiducial markers to track specific areas for site-specific microstructural correlative analysis. High resolution on-site microstructural analysis was performed on the left side of the nanoindentation grid to avoid the undesirable microstructural effect from the deeper indents.

For microstructural correlation, the surface perpendicular to the indentation loading axis was investigated using electron backscatter diffraction (EBSD). To capture the entire nanoindentation grid, low magnification EBSD was employed and to obtain local microstructural information in the vicinity of critical indents high magnification EBSD was performed. For the EBSD scanning, FEI Nova scanning electron microscope (SEM) operating at 20 kV and equipped with Hikari Super EBSD camera was utilized. To visualize the deformed volume under the tip, electron transparent foils were obtained precisely from the specific indents of interest using a FEI Nova 200 NanoLab dual beam focused ion beam SEM. The indented region was deposited with Pt to avoid localized thinning during milling and extraction of the foil. The foils were examined using FEI Technai G2 F20 transmission electron microscope (TEM) operating at 200 kV.

### 3. Results and discussion

#### 3.1. Mapping the phase and orientation dependent elastoplastic properties

A strong correlation between hardness map (obtained from Berkovich nanoindentation mapping) and phase map (generated from low magnification EBSD scans) is shown in Fig. 1(a,b). As specified earlier, the larger indents observed on the right side of the maps were added later for tracking specific indented region during the on-site microstructure correlative analysis. A disproportionately high hardness (>4.5 GPa) is observed in the region rich with martensite ( $\epsilon$ -h.c.p.) phases. Comparison of the hardness-contact depth ( $H-h$ ), force-contact depth ( $P-h$ ) and area-contact depth ( $A-h$ ) curves (Fig. 1(c,d)) of indent corresponding to  $\gamma$ -f.c.c. and  $\epsilon$ -h.c.p. explains this phase-dependency. The nanoindentation hardness is the ratio between resistance force ( $F$ ) and projected area ( $A$ ) under indent (area is by itself is a function of contact depth ( $h$ )). Note that with displacement-controlled indentation done under constant preload, the projected area remains constant (Fig. 1(c,d)) for every indent and the resistance force becomes the sole contributor to hardness. The observed hardness disparity occurred due to a large variation in the resistance force imparted by  $\gamma$ -f.c.c. and  $\epsilon$ -h.c.p. phases, which depends on multiple factors due to the dynamic elastoplastic deformation behavior of material during nanoindentation. A baseline force corresponding to elastic contact stress of the material under the tip is continuously registered [38]. According to Hertzian contact theory, the elastic force is a function of contact radius, indentation depth, and local elastic modulus, and therefore is orientation dependent. At incipient plasticity, a high force per area related to intrinsic resistance to plastic deformation is encountered, which contributes to very high hardness response at very low contact depth. This phenomenon is called indentation size effect (ISE) which is attributed to geometrically necessary dislocations (GNDs) generated to accommodate the indenter geometry [39]. Some research have suggested that ISE depends on lattice stability against shear [40,41]. First-principle quantification has reported higher lattice stress for  $\epsilon$ -h.c.p. phases in CrMnFeCoNi HEA compared to  $\gamma$ -f.c.c. phases [42].

After overcoming the critical lattice stress, cooperative displacement of multiple atomic planes results in the formation of dislocation loops. Typically slip progresses via rapid multiplication of dislocation loops (dislocation avalanches) during nanoindentation, which lowers the activation stress for further dislocation nucleation, thereby spontaneously reducing the hardness response [43]. The contribution of ISE to the hardness response reduces as the relative fraction of GND decreases and the fraction of statistically stored dislocations (SSD) such as dislocation loops increases with an increase in indentation depth [44]. The free energy required to generate the dislocation loops depends on the line energy of dislocation and SFE. However, in low SFE transformative HEA, formation of Shockley partial is energetically favored over dislocation loop during indentation and contributes to the SSD. Therefore, the continuous hardness reduction observed at higher depth in the present  $H-h$  curves can be attributed to formation and slip activities of partials, until disrupted by  $\gamma \rightarrow \epsilon$  martensitic transformation [45,46]. Due to limited slip propensity of  $\epsilon$ -h.c.p., twinning under the tip leads sudden stress relaxation, abruptly leading to intermittent sharp drops in the hardness response [47]. Dislocation pile-up at the twin interfaces subsequently enhances the instantaneous hardness response. A detailed account of the micromechanics of both the phases is provided subsequently in separate sections.

The nanoindentation experimentally provides reduced modulus ( $E_r$ ) which is contributed by the elastic deformation of both tip and sample and using equation (1), the elastic modulus ( $E$ ) of the sample is obtained.

$$\frac{1}{E_r} = \frac{1 - v^2}{E} + \frac{1 - v_i^2}{E_i} \quad (1)$$

where  $E_i$  is the modulus of diamond tip (1141 GPa) and  $v_i$  is its Poisson's ratio (0.22) [48]. The sample's Poisson's ratio ( $v$ ) is approximated as 0.26 from the values reported by Frank et. al [11] on a compositionally similar transformative HEA. The calculated modulus is mapped and presented alongside the EBSD inverse pole figure (IPF) map in Fig. 2. The microstructural dependency on modulus in the present sample is complex and depends on both phase and orientation. Furthermore, due to the heterogeneous nature of the microstructure the modulus corresponds to local combination of fine martensitic bands in the  $\gamma$ -f.c.c. phase. The orientation dependency of  $\gamma$ -f.c.c. phase align to crystal elasticity anisotropy as per generalized Hooke's law [49]. Due to the differences in lattice volume of  $\epsilon$ -h.c.p. and  $\gamma$ -f.c.c., a high degree of elastic misfit strain exists between these phases. Considering this hypothesis, the region containing closely spaced fine martensitic bands intertwined between  $\gamma$ -f.c.c. grains show very high modulus in the map.

#### 3.2. Incipient plasticity and nanoindentation induced phase transformation

For incipient plasticity study nanoindentation was performed using a spherically-conical indenter with a known tip radius of 5  $\mu\text{m}$ . The transition from Hertzian behavior marked by a pop-in event and indicates commencement of elastoplastic deformation behavior as the stresses under the tip reaches the critical values to produce Shockley partials. Mathematically, the maximum shear stress ( $\tau_m$ ) during incipient plasticity is expressed as:

$$\tau_m = 0.31 \left( \frac{6PE_r}{\pi^3 R^2} \right)^{1/3} \quad (2)$$

where  $E_r$  is the reduced modulus,  $R$  is the radius of the tip,  $P$  is the load under the tip during incipient plasticity. In the  $P-h$  curves corresponding to  $\gamma$ -f.c.c. phase with three different grain orienta-

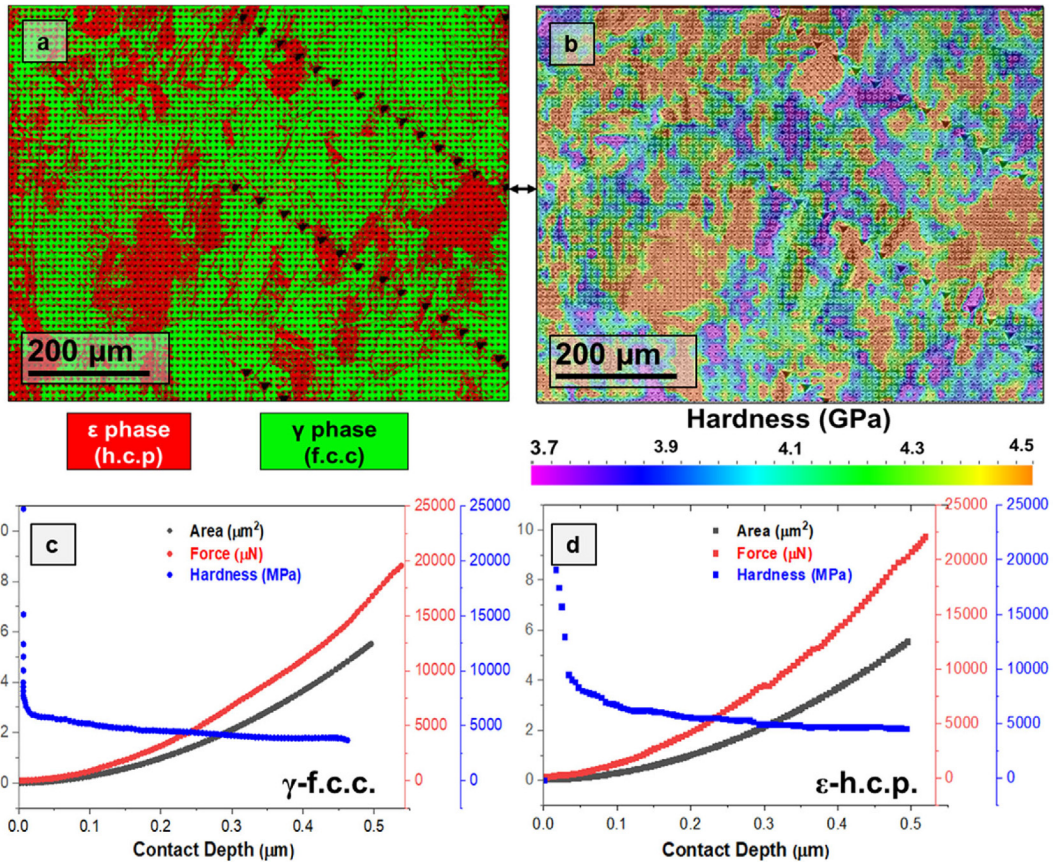


**Fig. 1.** Comparison of (a) phase distribution map obtained from EBSD, and (b) hardness map obtained from high-throughput Berkovich nanoindentation mapping. The phase dependency on hardness is investigated from force, area, and hardness variation with respect to the contact depth for (c)  $\gamma$ -f.c.c. and (d)  $\epsilon$ -h.c.p. phase.

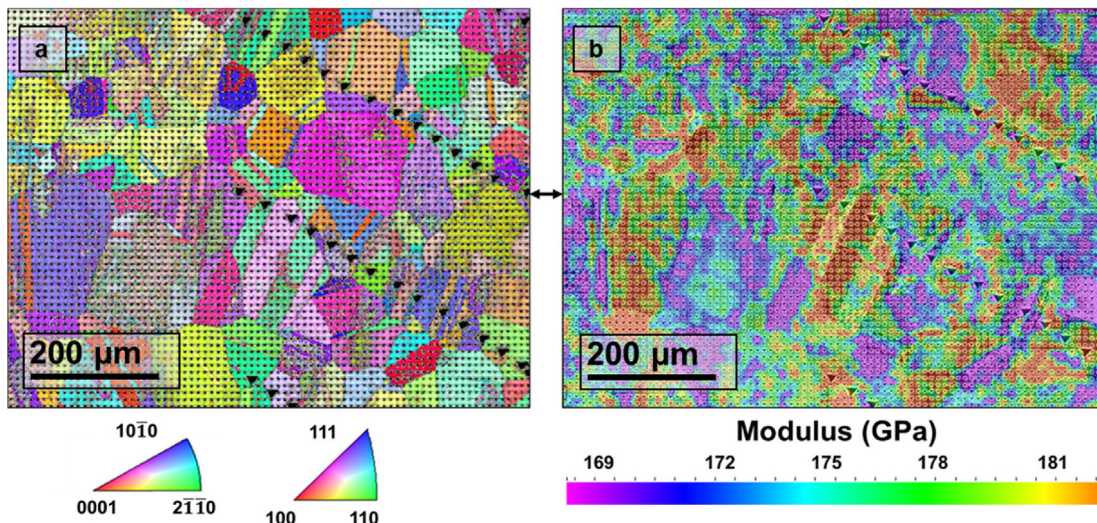


**Fig. 2.** Microstructure-micromechanical comparison shows complex relationship between (a) grain orientation (EBSD-IPF) map, and (b) modulus map obtained from Berkovich nanoindentation mapping.

tions (Fig. 3(a1-c1)), the pop-in event occurred at different critical load values. Using equation (2), the  $\tau_m$  for {111}, {110}, and {100} orientation is calculated as 15.1, 20.4 and 20.9 GPa, respectively. These values are greater than  $G_y/8$  which is theoretically sufficient to shear  $\gamma$ -f.c.c. ( $G_y = 76.8$  GPa [45] is shear strength of austenite iron) and generate sufficient Shockley partials. Apart from the crystal orientation, the incipient plasticity behavior of  $\gamma$ -f.c.c. is also

influenced by the heterogeneous distribution of fine martensitic bands in the  $\gamma$ -f.c.c. grain and depends on the arrangement of martensite in the  $\gamma$ -f.c.c. grain. For simplicity of analysis, the indent which corresponds predominately to a single phase is considered for this analysis (EBSD maps shown in Fig. 3(a3-c3)). Using the mathematical approach described by Pathak and Kalidindi [20], the nanoindentation stress strain ( $\sigma_i - \varepsilon_i$ ) relationship is deter-

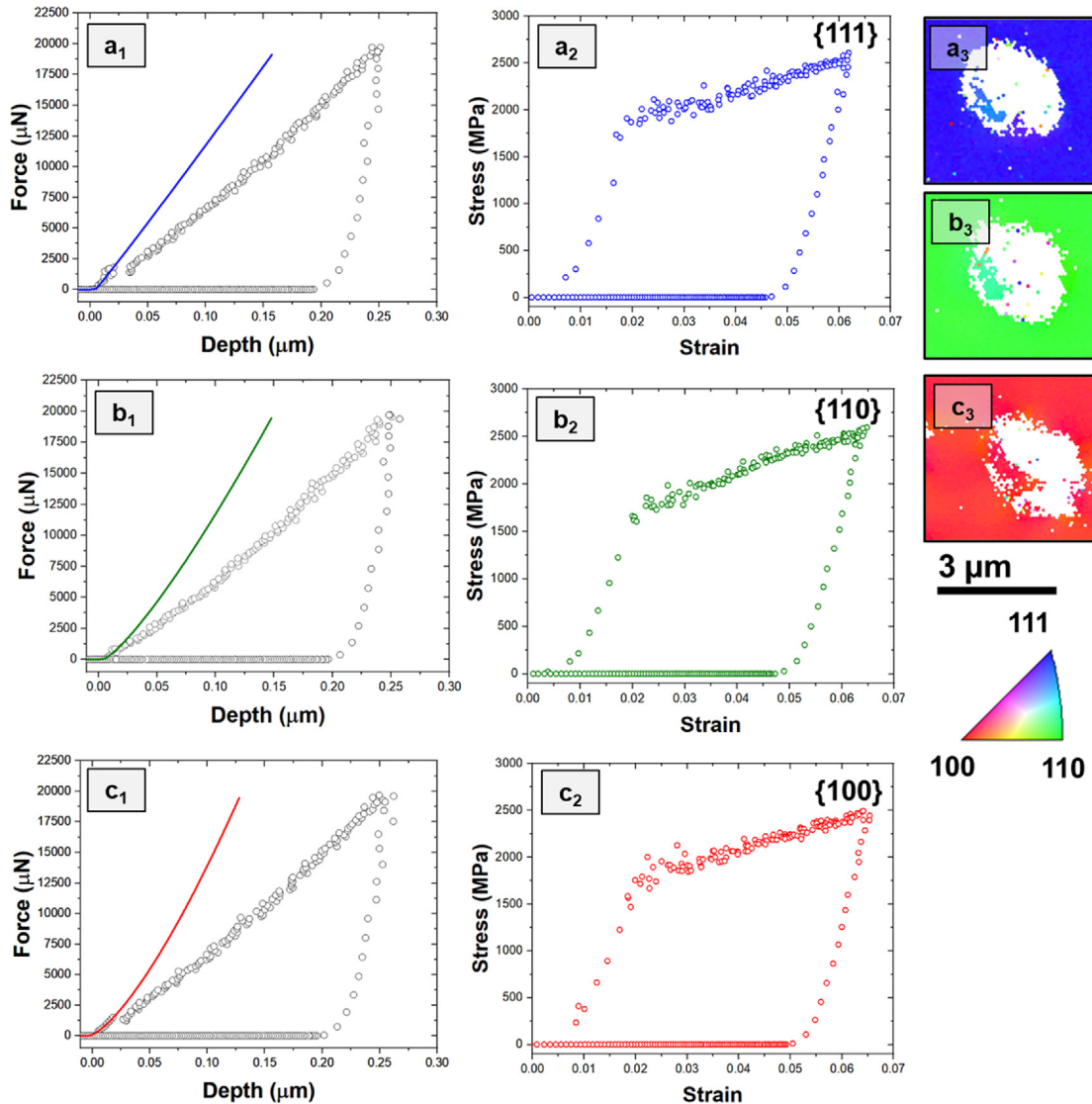


**Fig. 3.**  $P$ - $h$  curves (a1, b1, c1) and indentation stress-strain curves (a2, b2, c2) captured from interior of various  $\gamma$ -f.c.c. grains orientated along (a1, a2) {100}, (b1, b2) {110}, and (c1, c2) {111} directions using a spherico-conical indenter of 5  $\mu\text{m}$  tip diameter. The solid lines in the  $P$ - $h$  curve represent Hertzian elastic contact. The corresponding EBSD-IPF micrographs of the three orientations are shown in (a3, b3, c3).

mined from the  $P$ - $h$  curves and the  $\sigma_i - \varepsilon_i$  curves corresponding to three  $\gamma$ -f.c.c. crystal orientations are shown in Fig. 3(a2-c2). Pathak and Kalidindi [20] assumed indentation using a spherical geometry of tip radius  $R$  (5  $\mu\text{m}$  in the present investigation) to compression of a cylinder with radius equal to ' $a$ ' and height '2.4 $a$ '. Using this geometrical equivalency, the radius ' $a$ ' of the cylinder is approximated as,

$$a = \sqrt{2h_c R - h_c^2} \quad (3)$$

In the above equation,  $h_c$  is the contact depth of the indentation which is expressed as a function of maximum penetration depth ( $h_{max}$ ), maximum force at 98% of the unloading curve ( $F_{max}$ ), the slope of unloading curve between 40% and 98% of the unloading load ( $S$ ) and coefficient of proportionality  $\beta$  that equal to 0.72 for conical indenter (Eqn. (4)),

$$h_c = h_{max} - \beta \frac{F_{max}}{S} \quad (4)$$

The above assumption allows the indentation strain ( $\varepsilon_i$ ) to be idealized to classical form as the ratio between contracted height

(which is equal to plastic component of indentation penetration depth or  $h_p$ ) over original height of the cylinder (2.4 $a$ ) and is mathematically represented as,

$$\varepsilon_i = \frac{h_p}{2.4a} \quad (5)$$

Note that penetration depth equals to maximum depth ( $h_{max}$ ) when nanoindentation introduces plastic deformation, but in the elastic deformation regime, it is equivalent to the elastic depth calculated by Oliver-Pharr approach ( $h_{max}$  – total depth). Similarly, the indentation stress ( $\sigma_i$ ) is attributed as the ratio between instantaneous load ( $P$ ) and initial area of the cylindrical face, and is expressed as,

$$\sigma_i = \frac{P}{\pi a^2} \quad (6)$$

The slope of the linear portion of the  $\sigma_i - \varepsilon_i$  curves (Fig. 3(a2-c2)) represent the effective modulus of the three crystal orientations, which is found to be 133, 131, 114 GPa for {111}, {110}, and {100}, respectively, and agree with Hooke's relationship of crystal elastic anisotropy that was observed earlier in the modulus

map (Fig. 2). Following the linear elastic part, a region of uncertainty is observed in the  $\sigma_i - \varepsilon_i$  curves, which is attributed to contact discontinuity noted during pop-in event in the  $P-h$  curves. This region of uncertainty is succeeded by the onset of plastic deformation. The nanoindentation yield stress is found to be lowest for the {111} orientation, followed by the {110} and {100} grains. Being the most closed pack orientation, the grains with {111} crystal orientation plasticizes at a lower shear stress (Eqn. (2)), which results in its lower yield stress.

Fig. 4(a-c) shows the  $P-h$  characteristics corresponding to Berkovich indentation for the three primary crystal orientations. Quite contrary to  $P-h$  curves of the spherically-conical indentation (Fig. 3), the Berkovich tip shows a steady breakaway from pure elastic behavior (Hertzian curve). The separation occurs at different force and depth for the three different  $\gamma$ -f.c.c. orientations, which is indicative of the orientation dependent in incipient plasticity earlier reported from spherically-conical indentation. The hardness corresponding to the {111} grain is observed to be lower than the remaining two orientations. This coincides with Tabor's empirical rule and the nanoindentation hardness corresponding to Berkovich indentation is found to be proportional to the local yield stress [50]. However, the  $P-h$  characteristics at incipient plasticity do not demonstrate the characteristic pop-in as detected during the spherical indentation because of one or more of the following reasons: (i) annealing at 800 °C for 30 min may not be sufficient to fully annihilate dislocations and due to these pre-existing dislocations the incipient plasticity is not a spontaneous event under Berkovich tip, (ii) relatively higher loading rate of 0.2  $\mu\text{m}/\text{s}$  falls short to fully resolve the dislocation activities under the tip [51], and (iii)

the sharp tip radius (<50 nm) of Berkovich indenter confines the spherical portion of contact depth to approximately less than 100 nm, resulting in the stress state to be multiaxial during incipient plasticity.

Following the breakaway from Hertzian behavior, a subsequent pop-in event is noticed at higher load/depth, which most likely corresponds to a spontaneous  $\gamma \rightarrow \varepsilon$  martensitic transformation. Due to smaller interaction volume and sharp angle (65.3°) of the Berkovich tip, the indentation contact pressure can reach the critical transformation pressure to initiate the phase transformation. Nanoindentation induced phase transformation using Berkovich tip has been well reported by multiple researchers [45,46]. The martensite formation leads to a sudden volume change [52] and spontaneous dislocation multiplication due to creation of new coherent interfaces under the tip resulting the pop-in event. Ahn *et al.* [46] described TRIP as nucleation-controlled process and the associated pop-in as a reaction to maintain a constant loading rate during the transformation. Interestingly, indents located near the grain boundary plasticize at much higher load followed by an immediate pop-in event (Fig. 4(d)). This is attributed to geometrical constraints imposed by the grain boundaries to the dislocation (Shockley partials) motion that increases the critical stress for incipient plasticity and promotes accelerated nanoindentation induced TRIP immediately after incipient plasticity due to availability of a large concentration of partials in smaller volume. The ratio between pop-in force and displacement corresponds to energy released due to the martensitic transformation under the tip [53], and is a quantitative indicator of TRIP propensity. Data points corresponding to the three f.c.c. grain orientations are linear

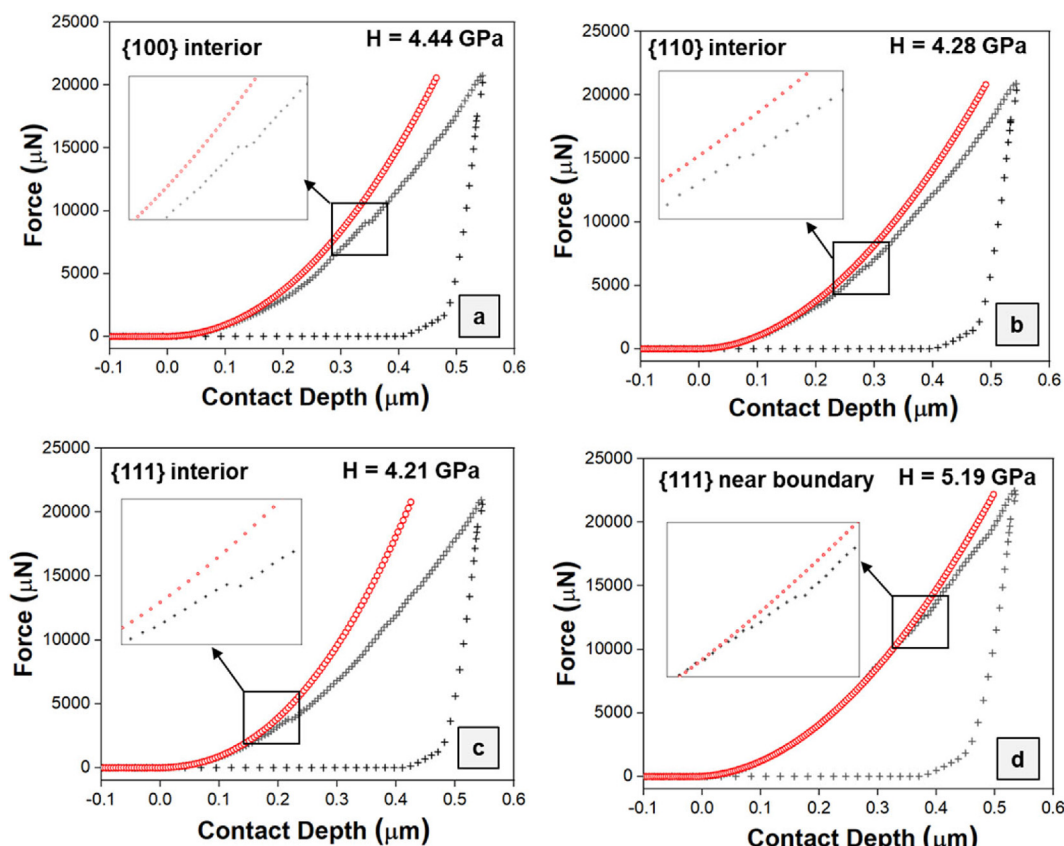


**Fig. 4.**  $P-h$  curves corresponding to Berkovich indenter captured from interior of various  $\gamma$ -f.c.c. grains orientated along (a) {100}, (b) {110}, and (c) {111} directions show a gradual deviation from Hertzian elastic behavior (red curves) followed by a pop-in (clearer in insets) due to TRIP, (d)  $P-h$  curve captured near the boundary of {111} grain shows TRIP induced pop-in soon after the incipient plasticity. Note the hardness ( $H$ ) corresponding to each  $P-h$  curve in mentioned in the top right part of the curve. (For interpretation of the references to color in this figure legend, the reader is referred to the web version of this article.)

fitted and compiled in Fig. 5(a). Despite the high scatter in the pop-in analysis, the goodness of fit ( $R^2$ ) in the linear regression is found to be less than one for all the three orientations, which indicates high confidence of data fitting. The slopes are found to be 33584, 21,973, 20,752  $\mu\text{N}/\mu\text{m}$  for {111}, {110} and {100} orientation. This denotes that TRIP propensity follows the order of {111} > {110} > {100}, as the net stability after martensitic transformation is proportional to the energy released during TRIP. The transformed martensite is visualized in the region under the tip in the TEM micrograph (Fig. 5(b)). The orientation relationship between the parent grain (untransformed region) and transformed region is indexed in the selective area diffraction (SAD) pattern shown in Fig. 5(c1, c2). The  $\gamma$ -f.c.c. grain shown in the TEM corresponds to [112] zone axis with  $\vec{g}$  along the 001 direction. The TEM micrograph and SAD analysis confirm the presence of residual nanoscaled  $\varepsilon$ -h.c.p. (oriented along  $\bar{2}\bar{1}\bar{1}\bar{0}$  direction) interspersed with the parent untransformed  $\gamma$ -f.c.c. grain. Nanoindentation induced TRIP forms  $\varepsilon$ -h.c.p. dominated region right under the tip and along the Berkovich faces. Reduction in spacing of diffraction spots in the corresponding SAD pattern (Fig. 5(c2)) corroborates with extensive phase transformation under the tip. Fine lenticular shaped deformation twins are observed in these newly formed  $\varepsilon$ -h.c.p. and they are densely decorated with dislocations. Formation of twins with ultrafine spacing in the newly formed  $\varepsilon$ -h.c.p. under the tip are inferred from the signature streaks observed in SAD pattern (Fig. 5(c1)). Furthermore, a non-linear behavior is observed just after the pop-in in the  $P$ - $h$  curves due to localized stress relaxation associated with TWIP inside the newly formed  $\varepsilon$ -h.c.p. under the tip [43]. Contrary to the spontaneity of strain induced phase transformation, the twinning process under the tip is a non-

spontaneous process and does not demonstrate pop-in behavior. Note that rapid dislocation accumulation in the coherent twin boundaries can also lead to subsequent pop-in events. However, such pop-ins are rarely observed in the  $\gamma$ -f.c.c. grains.

### 3.3. Deformation twinning mechanism of martensite under nanoindentation

The complex deformation behavior of  $\varepsilon$ -h.c.p. in this HEA is multifaceted and depends on the relation of the nanoindentation loading axis with c-axis of the  $\varepsilon$ -h.c.p. crystal. Due to less-than-ideal  $c/a$  (1.633) of the present HEA composition [54], twins are favorable when tensile loads are applied parallel to the prismatic planes, or compressive load is applied parallel to the basal plane [55,56]. The multiaxial stress field induced by the Berkovich tip geometry further heightens the complexity of nanoindentation induced twinning phenomenon. At very low depth of indentation, the spherical part of the Berkovich tip will be in contact and therefore, the stress state may be compression dominated under the tip.

Pure compressive loading along the c-axis activates  $\{10\bar{1}1\} < 10\bar{1}2$  > compressive twins and  $<\text{c} + \text{a}>$  dislocations [7]. For the basal orientation, the first pop-in is observed in  $P$ - $h$  curve (Fig. 6(a)) at very low depth during which the martensite may be in a compression dominated stress state, and the pop-in arises mainly due to generation of compression twins and rapid dislocation activities along the twin interfaces. However, at higher depth of indentation, multiaxial stress field is imparted by the Berkovich faces. Under this condition, tensile twinning under the tip and/or along the faces gets activated [56]. High magnification EBSD (Fig. 6(b)) done on the indented surface shows presence of sheared zone with 86°

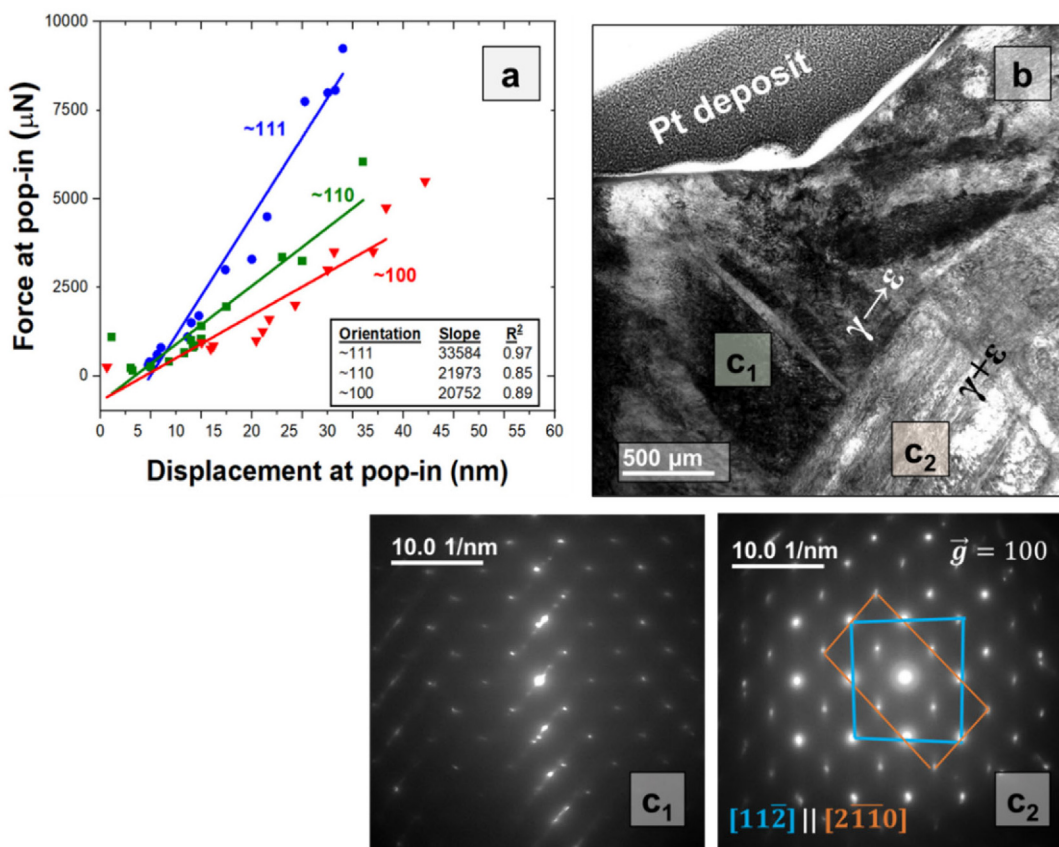


**Fig. 5.** Phase transformation during nanoindentation. (a) slope of pop-in force to displacement curves represents energy released during nanoindentation induced TRIP and shows orientation dependency, (b) TEM micrograph corresponding to  $\gamma$ -f.c.c. (interspersed with fine martensites) shows extensive TRIP effect under the Berkovich tip, (c1, c2) SAD corresponding to transformed and untransformed region under the tip as marked in (b).

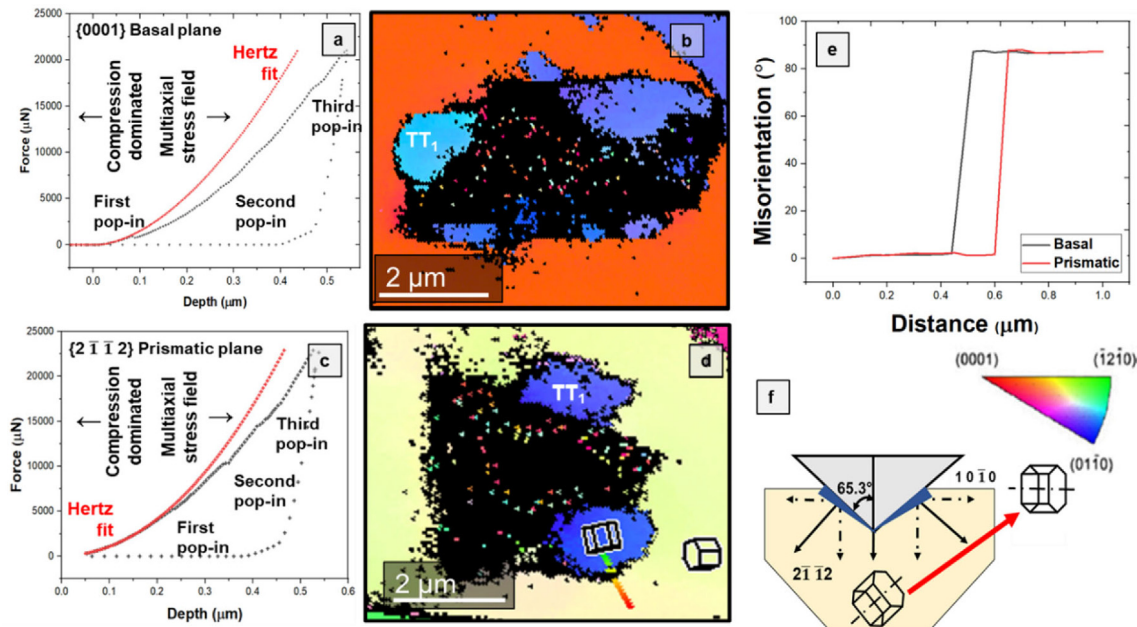


**Fig. 6.** Nanoindentation deformation behavior in martensite. (a)  $P$ - $h$  curve corresponding to Berkovich nanoindentation of  $\varepsilon$ -h.c.p. with basal {0001} orientation, (b) EBSD micrograph of surface normal to nanoindentation axis, (c)  $P$ - $h$  curve corresponding to Berkovich nanoindentation of prismatic  $\{2\bar{1}\bar{1}2\}$  orientation, (d) high magnification EBSD of the surface normal showing TT<sub>1</sub>, (e) misorientation profile of the TT<sub>1</sub> with respect to basal and prismatic orientation, and (f) schematic illustrating the mechanism of twinning due to multiaxial stress field under the Berkovich tip during nanoindentation.

misorientation typically associated with type-1 tensile twin (TT<sub>1</sub>) with  $\{10\bar{1}2\} < 10\bar{1}1 >$  orientation [54]. The  $P$ - $h$  curve corresponding to  $\{2\bar{1}\bar{1}2\}$  prismatic orientation (Fig. 6(c)) shows multiple pop-ins and non-linear excursions at higher load/depth. High magnification EBSD (Fig. 6(d)) reveals region with  $86^\circ$  misorientation on the edge of the indents oriented in  $\{10\bar{1}0\}$  direction. Some differences between plastic deformation of prismatic and basal orientation are observed: (i) the incipient plasticity occurs at greater load for the prismatic orientation due to its higher critical resolved shear stress compared to basal plane, (ii) incipient plasticity occurs in the presence of multiaxial stress field and leads to simultaneous activation of multiple twin systems.

TEM micrograph of the region under the tip corresponding to basal orientation is represented in Fig. 7. The TEM micrograph and SAD pattern confirms the presence of type-1 compression twin (CT<sub>1</sub>) with  $\{10\bar{1}1\} < 10\bar{1}2 >$  orientation relationship under the tip (Fig. 7(a)) and sub-surface evidence of TT<sub>1</sub> along the Berkovich face (Fig. 7(b)). The region right under the tip predominately undergoes compression loading and interacts with the spherical portion of the Berkovich tip. The twinned region along the Berkovich faces contain substructures with morphology due to “twin bridging phenomenon” as reported by Sinha *et al.* [54] due to multiaxial tensile stress field imparted by the Berkovich faces. The zigzag network of twins was observed  $45\text{--}50^\circ$  from the martensitic boundary, with high average misorientation of  $86^\circ$  with respect to the base martensitic orientation as confirmed from the misorientation line scan (Fig. 6(e)).

#### 3.4. Machine learning based clustering indicates phase-dependent work hardening

Based on the above investigation, key differences in deformation characteristics of  $\varepsilon$ -h.c.p. compared to  $\gamma$ -f.c.c. are: (i) copious twinning provides coherent sites for rapid dislocation activities in  $\varepsilon$ -h.c.p., (ii) swift breakaway from Hertzian elastic behavior due to twin dominated dislocation activities under the tip, and

(iii) frequent pop-in and non-linear excursion activities related to TWIP. These observations indicate the possibility of a higher degree of local work hardening in the  $\varepsilon$ -h.c.p. rich region compared to the  $\gamma$ -f.c.c. phases. A mathematical relationship formulated by Cheng *et. al* [57] (Equation (7)) relates hardness and modulus ratio ( $H/E$ ) to the ratio between irreversible work ( $W_u$ ) and total work ( $W_t$ ).  $W_u$  is related to energy dissipated into the local volume and  $W_t$  includes both the elastic and plastic work done under the tip,  $\Pi_\theta$  is a dimensionless factor of proportionality,

$$\frac{H}{E} \approx \Pi_\theta \left( 1 - \frac{W_u}{W_t} \right) \quad (7)$$

Hardness depends on both intrinsic factors such as lattice stress and critical shear stress of material under the tip, and extrinsic factor which influences the dislocation storage capability of the material during indentation. On the other hand, modulus only depends on intrinsic factors and remains unaffected during plastic deformation. Since the nanoindentation is displacement-controlled, fundamentally higher  $H/E$  indicates that the activation material volume under the tip has greater dislocation storage capability, which suggests greater work hardening capacity for region with higher  $H/E$ . Mapping  $H/E$  intuitively provides spatial variation of work hardening in the dual-phase HEA (Fig. 8(a)). Gaussian mixture model (GMMs) is a type of machine learning algorithm used to classify data into different categories based on the probability distribution. Compared to multiple similarity-based clustering, GMM clustering is preferred for its greater statistical maturity, ability to create flexible soft partition between clusters and assign probabilistic labels [58]. The accuracy of the classification improves with the volume of data, making large nanoindentation map suitable dataset to be augmented into such machine learning techniques. GMM clustering method was used to delineate the region of high and low work hardening from the  $H/E$  map. Machine learning module integrated in FemtoTools data analysis software was used for the GMM clustering. Two clusters have been defined using hardness and modulus data (due to lowest silhouette score for two clusters for the present dataset), and the limiting  $H/E$  value corresponding to each

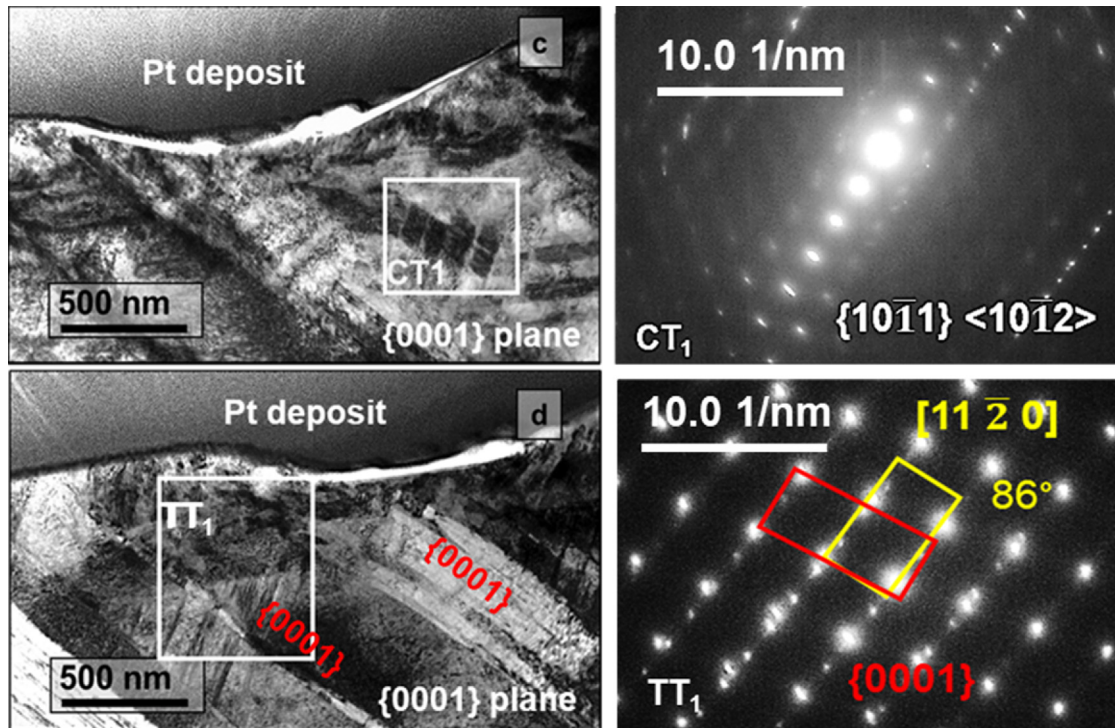


**Fig. 7.** Site-specific TEM investigation illustrates microstructural impact of Berkovich nanoindentation on  $\epsilon$ -h.c.p. with basal  $\{0001\}$  orientation (a, b) TEM image and SAD pattern captures twin mechanism occurred under the tip and along the Berkovich faces.

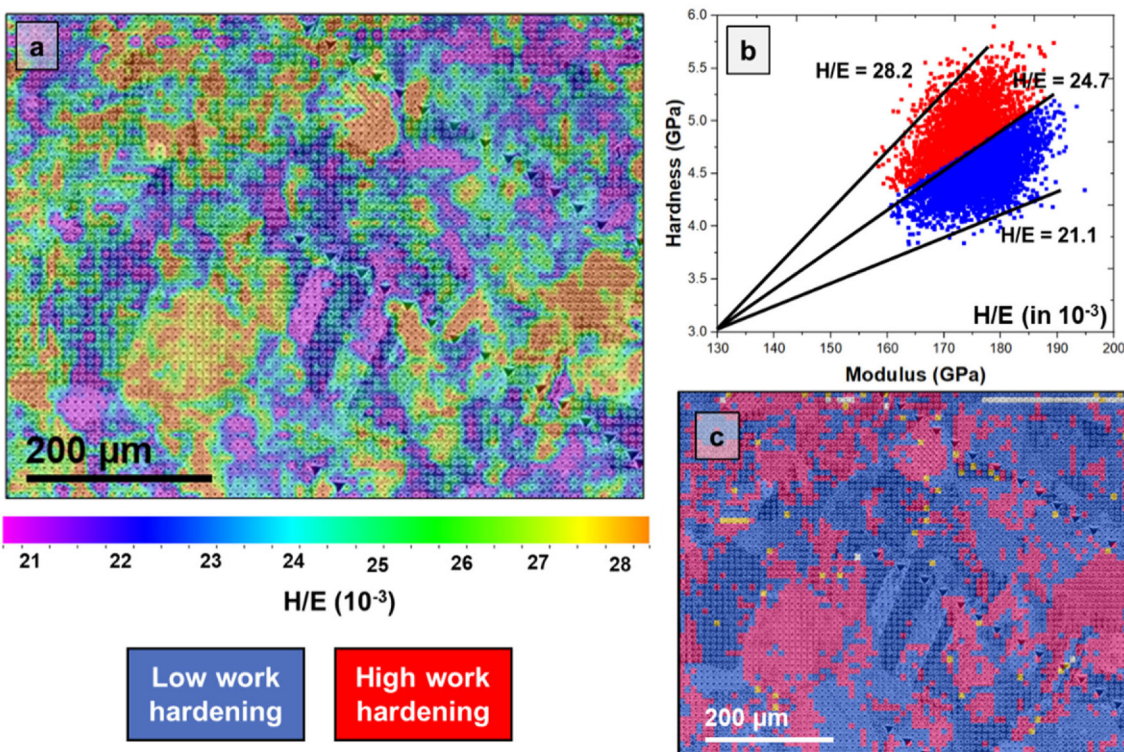


**Fig. 8.** Mapping work hardening in the transformative HEA by machine learning based clustering. (a)  $H/E$  map, (b) GMM based clustering using the hardness and modulus data, and (c) cluster map shows strong resemblance with phase distribution.

cluster was determined and mapped (Fig. 8(b,c)). Note that the GMM clustering algorithm, being a nearest centroid classifier, detects outliers by identifying datapoints in low-density regions. These points are marked in yellow color in the cluster map and

are eliminated from further analysis. The cluster map shows a strong correlation to the phase distribution. Therefore, the map statistically validates the higher work hardening tendency in  $\epsilon$ -h.c.p. phase due to non-slip-based deformation mechanisms com-

pared to the slip-based deformation in  $\gamma$ -f.c.c. phase. Furthermore, the high work hardening region extends near the grain boundaries of the  $\gamma$ -f.c.c. phase, due to increased TRIP propensity arising from geometrical constraints introduced by the grain boundaries.

#### 4. Conclusions

High-resolution nanoindentation mapping augmented with machine learning based clustering provided multifaceted insights into the complex hierarchical and heterogenous deformation micromechanics of a transformative HEA. The austenite ( $\gamma$ -f.c.c.) and martensite ( $\epsilon$ -h.c.p.) grains deform via distinctive mechanisms. Slip-based deformation dominates in the  $\gamma$ -f.c.c. phase, with elastic properties and incipient plasticity showing strong orientation dependency. The deviation from Hertzian elastic behavior indicates incipient plasticity via homogenous dislocation activities under the tip. The deformation micromechanics varies spatially within the same grain. Geometric constraints imposed by grain boundaries result in intense dislocation localization and rapid dislocation burst resulting from significant  $\gamma \rightarrow \epsilon$  transformation under the tip. On the other hand, deformation in  $\epsilon$ -h.c.p. is twin-dominated, and the twin boundaries act as coherent dislocation activation sites for dislocation activities during nanoindentation. Both compression and tensile twins formed depending on the orientation relationship of c-axis with the nanoindenter loading direction. Use of H/E ratio and GMM clustering was effective in mapping and classifying the work hardening and shows strong phase dependency.

#### CRediT authorship contribution statement

**Abhijeet Dhal:** Conceptualization, Methodology, Formal analysis, Validation, Investigation, Data curation, Visualization, Writing – original draft. **Ravi Sankar Haridas:** Formal analysis, Writing – review & editing. **Priyanka Agrawal:** Formal analysis, Methodology, Investigation, Writing – review & editing. **Sanya Gupta:** Investigation. **Rajiv S. Mishra:** Conceptualization, Funding acquisition, Formal analysis, Writing – review & editing.

#### Data availability

Data will be made available on request.

#### Declaration of Competing Interest

The authors declare that they have no known competing financial interests or personal relationships that could have appeared to influence the work reported in this paper.

#### Acknowledgements

The authors acknowledge Materials Research Facility at University of North Texas for access to electron microscopes. The feedback provided by Dr. Roman Mouginot, Application Scientist, Femto-Tools AG is highly acknowledged. This work was supported by the DEVCOM Army Research Laboratory under Cooperative Agreement #W911NF-18-2-0067.

#### Data availability statement

The raw/processed data required to reproduce these findings cannot be shared at this time as the data also forms part of an ongoing study.

#### References

- [1] R.S. Mishra, R.S. Haridas, P. Agrawal, High entropy alloys – Tunability of deformation mechanisms through integration of compositional and microstructural domains, Mater. Sci. Eng. A. 812 (2021), <https://doi.org/10.1016/j.msea.2021.141085> 141085.
- [2] R.S. Haridas, P. Agrawal, S. Yadav, P. Agrawal, A. Gumaste, R.S. Mishra, Work hardening in metastable high entropy alloys: a modified five-parameter model, J. Mater. Res. Technol. 18 (2022) 3358–3372, <https://doi.org/10.1016/j.jmrt.2022.04.016>.
- [3] M. Frank, S.S. Nene, Y. Chen, S. Thapliyal, S. Shukla, K. Liu, S. Sinha, T. Wang, M.J. Frost, K. An, R.S. Mishra, Direct evidence of the stacking fault-mediated strain hardening phenomenon, Appl. Phys. Lett. 119 (2021), <https://doi.org/10.1063/5.0062153>.
- [4] P. Agrawal, S. Gupta, S. Shukla, S.S. Nene, S. Thapliyal, M.P. Toll, R.S. Mishra, Role of Cu addition in enhancing strength-ductility synergy in transforming high entropy alloy, Mater. Des. 215 (2022), <https://doi.org/10.1016/j.matdes.2022.110487> 110487.
- [5] X.D. Xu, P. Liu, Z. Tang, A. Hirata, S.X. Song, T.G. Nieh, P.K. Liaw, C.T. Liu, M.W. Chen, Transmission electron microscopy characterization of dislocation structure in a face-centered cubic high-entropy alloy Al0.1CoCrFeNi, Acta Mater. 144 (2018) 107–115, <https://doi.org/10.1016/j.actamat.2017.10.050>.
- [6] F. Otto, A. Dlouhý, C. Somsen, H. Bei, G. Eggerer, E.P. George, The influences of temperature and microstructure on the tensile properties of a CoCrFeMnNi high-entropy alloy, Acta Mater. 61 (2013) 5743–5755, <https://doi.org/10.1016/j.actamat.2013.06.018>.
- [7] M.H. Yoo, Slip, twinning, and fracture in hexagonal close-packed metals, Metall. Trans. A. 12 (1981) 409–418, <https://doi.org/10.1007/BF02648537>.
- [8] A. Dhal, B. Prathyusha, R. Kumar, S.K. Panigrahi, Twin evolution and work-hardening phenomenon of a bulk ultrafine grained copper with high thermal stability and strength-ductility synergy, Mater. Sci. Eng. A. 802 (2021), <https://doi.org/10.1016/j.msea.2020.140622> 140622.
- [9] S.S. Nene, P. Agrawal, M. Frank, A. Watts, S. Shukla, C. Morphew, A. Chesetti, J.S. Park, R.S. Mishra, Transformative high entropy alloy conquers the strength-ductility paradigm by massive interface strengthening, Scr. Mater. 203 (2021), <https://doi.org/10.1016/j.scriptamat.2021.114070> 114070.
- [10] R.S. Haridas, P. Agrawal, S. Thapliyal, S. Yadav, R.S. Mishra, B.A. McWilliams, K. Cho, Strain rate sensitive microstructural evolution in a TRIP assisted high entropy alloy: Experiments, microstructure and modeling, Mech. Mater. 156 (2021), <https://doi.org/10.1016/j.mechmat.2021.103798> 103798.
- [11] M. Frank, Y. Chen, S.S. Nene, S. Sinha, K. Liu, K. An, R.S. Mishra, Investigating the deformation mechanisms of a highly metastable high entropy alloy using in-situ neutron diffraction, Mater. Today Commun. 23 (2020), <https://doi.org/10.1016/j.mtcomm.2019.100858> 100858.
- [12] M. Frank, S.S. Nene, Y. Chen, B. Gwalani, E.J. Kautz, A. Devaraj, K. An, R.S. Mishra, Correlating work hardening with co-activation of stacking fault strengthening and transformation in a high entropy alloy using in-situ neutron diffraction, Sci. Rep. 10 (2020) 1–10, <https://doi.org/10.1038/s41598-020-79492-8>.
- [13] Y. Hu, L. Shu, Q. Yang, W. Guo, P.K. Liaw, K.A. Dahmen, J.M. Zuo, Dislocation avalanche mechanism in slowly compressed high entropy alloy nanopillars, Commun. Phys. 1 (2018) 1–8, <https://doi.org/10.1038/s42005-018-0062-z>.
- [14] S. Peng, K. Jin, X. Yi, Z. Dong, X. Guo, Y. Liu, Y. Cheng, N. Jia, H. Duan, J. Xue, Mechanical behavior of the HfNbZrTi high entropy alloy after ion irradiation based on micro-pillar compression tests, J. Alloys Compd. 892 (2022), <https://doi.org/10.1016/j.jallcom.2021.162043> 162043.
- [15] Q. Zhang, R. Huang, X. Zhang, T. Cao, Y. Xue, X. Li, Deformation Mechanisms and Remarkable Strain Hardening in Single-Crystalline High-Entropy-Alloy Micropillars/Nanopillars, Nano Lett. 21 (2021) 3671–3679, <https://doi.org/10.1021/acs.nanolett.1c00444>.
- [16] Z. Fu, L. Jiang, J.L. Wardini, B.E. MacDonald, H. Wen, W. Xiong, D. Zhang, Y. Zhou, T.J. Rupert, W. Chen, E.J. Lavernia, A high-entropy alloy with hierarchical nanoprecipitates and ultrahigh strength, Sci. Adv. 4 (2018) 1–9, <https://doi.org/10.1126/sciadv.aat8712>.
- [17] P. Fan, N.K. Katiyar, X. Zhou, S. Goel, Uniaxial pulling and nano-scratching of a newly synthesized high entropy alloy, APL Mater. 10 (2022), <https://doi.org/10.1063/5.0128135>.
- [18] S. Sinha, R.A. Mirshams, T. Wang, S.S. Nene, M. Frank, K. Liu, R.S. Mishra, Nanoindentation behavior of high entropy alloys with transformation-induced plasticity, Sci. Rep. 9 (2019) 1–11, <https://doi.org/10.1038/s41598-019-43174-x>.
- [19] S. Pathak, J. Michler, K. Wasmer, S.R. Kalidindi, Studying grain boundary regions in polycrystalline materials using spherical nano-indentation and orientation imaging microscopy, J. Mater. Sci. 47 (2012) 815–823, <https://doi.org/10.1007/s10853-011-5859-z>.
- [20] S. Pathak, S.R. Kalidindi, Spherical nanoindentation stress-strain curves, Mater. Sci. Eng. R Reports. 91 (2015) 1–36, <https://doi.org/10.1016/j.mser.2015.02.001>.
- [21] A.A. Martin, J.A. Hammons, H.B. Henderson, N.P. Calta, M.H. Nielsen, C.C. Cook, J. Ye, A.A. Maich, N.E. Teslich, T.T. Li, M.J. Thompson, M.F. Besser, M.J. Matthews, R.T. Ott, O. Rios, S.K. McCall, T.M. Willey, J.R.I. Lee, Enhanced mechanical performance via laser induced nanostructure formation in an additively manufactured lightweight aluminum alloy, Appl. Mater. Today. 22 (2021), <https://doi.org/10.1016/j.apmt.2021.100972> 100972.

- [22] S. Janakiram, P.S. Phani, G. Ummethala, S.K. Malladi, J. Gautam, L.A.I. Kestens, New insights on recovery and early recrystallization of ferrite-pearlite banded cold rolled high strength steels by high speed nanoindentation mapping, *Scr. Mater.* 194 (2021), <https://doi.org/10.1016/j.scriptamat.2020.113676> 113676.
- [23] Y. Xiao, H. Besharatloo, B. Gan, X. Maeder, R. Spolenak, J.M. Wheeler, Combinatorial investigation of Al-Cu intermetallics using small-scale mechanical testing, *J. Alloys Compd.* 822 (2020), <https://doi.org/10.1016/j.jallcom.2019.153536> 153536.
- [24] A. Dhal, S. Thapliyal, S. Gaddam, P. Agrawal, R.S. Mishra, Multiscale hierarchical and heterogeneous mechanical response of additively manufactured novel Al alloy investigated by high-resolution nanoindentation mapping, *Sci. Rep.* 12 (2022) 1–8, <https://doi.org/10.1038/s41598-022-23083-2>.
- [25] A. Dhal, P. Agrawal, R.S. Haridas, S. Gaddam, A. Sharma, D. Parganiha, R.S. Mishra, H. Kawanaka, S. Matsushita, Y. Yasuda, S.H.C. Park, W. Yuan, High-Throughput Investigation of Multiscale Deformation Mechanism in Additively Manufactured Ni Superalloy, *Metals (Basel.)* 13 (2023) 1–17, <https://doi.org/10.3390/met13020420>.
- [26] Y. Tong, H. Zhang, H. Huang, L. Yang, Y. Hu, X. Liang, M. Hua, J. Zhang, Strengthening mechanism of CoCrNiMox high entropy alloys by high-throughput nanoindentation mapping technique, *Intermetallics*, 135 (2021), <https://doi.org/10.1016/j.intermet.2021.107209> 107209.
- [27] S. Muskeri, B. Gwalani, S. Jha, A. Yu, P.A. Jannotti, R.S. Haridas, B.E. Schuster, J.T. Lloyd, R.S. Mishra, S. Mukherjee, Excellent ballistic impact resistance of Al<sub>0.3</sub>CoCrFeNi multi-principal element alloy with unique bimodal microstructure, *Sci. Rep.* 11 (2021) 1–12, <https://doi.org/10.1038/s41598-021-02209-y>.
- [28] H. Besharatloo, J.M. Wheeler, Influence of indentation size and spacing on statistical phase analysis via high-speed nanoindentation mapping of metal alloys, *J. Mater. Res.* 36 (2021) 2198–2212, <https://doi.org/10.1557/s43578-021-00214-5>.
- [29] E.P. Koumoulos, K. Paraskevoudis, C.A. Charitidis, Constituents phase reconstruction through applied machine learning in nanoindentation mapping data of mortar surface, *J. Compos. Sci.* 3 (2019), <https://doi.org/10.3390/jcs3030063>.
- [30] B. Vignesh, W.C. Oliver, G.S. Kumar, P.S. Phani, Critical assessment of high speed nanoindentation mapping technique and data deconvolution on thermal barrier coatings, *Mater. Des.* 181 (2019), <https://doi.org/10.1016/j.matdes.2019.108084> 108084.
- [31] G. Konstantopoulos, E.P. Koumoulos, C.A. Charitidis, Classification of mechanism of reinforcement in the fiber-matrix interface: Application of Machine Learning on nanoindentation data, *Mater. Des.* 192 (2020), <https://doi.org/10.1016/j.matdes.2020.108705> 108705.
- [32] Z. Liu, J. Zhang, B. He, Y. Zou, High-speed nanoindentation mapping of a near-alpha titanium alloy made by additive manufacturing, *J. Mater. Res.* 36 (2021) 2223–2234, <https://doi.org/10.1557/s43578-021-00204-7>.
- [33] X. Xiao, L. Yu, Nano-indentation of ion-irradiated nuclear structural materials: A review, *Nucl. Mater. Energy.* 22 (2020), <https://doi.org/10.1016/j.nme.2019.100721> 100721.
- [34] S. Gupta, P. Agrawal, S.S. Nene, R.S. Mishra, Friction stir welding of  $\gamma$ -fcc dominated metastable high entropy alloy: Microstructural evolution and strength, *Scr. Mater.* 204 (2021), <https://doi.org/10.1016/j.scriptamat.2021.114161> 114161.
- [35] W.J. Zong, D. Wu, C.L. He, Radius and angle determination of diamond Berkovich indenter, *Meas. J. Int. Meas. Confed.* 104 (2017) 243–252, <https://doi.org/10.1016/j.measurement.2017.03.035>.
- [36] P. Sudharshan Phani, W.C. Oliver, A critical assessment of the effect of indentation spacing on the measurement of hardness and modulus using instrumented indentation testing, *Mater. Des.* 164 (2019), <https://doi.org/10.1016/j.matdes.2018.107563> 107563.
- [37] W.C. Oliver, G.M. Pharr, Measurement of hardness and elastic modulus by instrumented indentation: Advances in understanding and refinements to methodology, *J. Mater. Res.* 19 (2004) 3–20, <https://doi.org/10.1557/jmr.2004.19.1.3>.
- [38] A. Fischer-Cripps, K. Johnson, Introduction to Contact Mechanics, *Mech. Eng. Series* (2002), <https://doi.org/10.1115/1.1470678>.
- [39] W.D. Nix, H. Gao, Indentation size effects in crystalline materials: A law for strain gradient plasticity, *J. Mech. Phys. Solids*. 46 (1998) 411–425, [https://doi.org/10.1016/S0022-5096\(97\)00086-0](https://doi.org/10.1016/S0022-5096(97)00086-0).
- [40] H. Jang, D. Farkas, Interaction of lattice dislocations with a grain boundary during nanoindentation simulation, *Mater. Lett.* 61 (2007) 868–871, <https://doi.org/10.1016/j.matlet.2006.06.004>.
- [41] S.V. Dmitriev, J. Li, N. Yoshikawa, Y. Shibutani, Theoretical strength of 2D hexagonal crystals: Application to bubble raft indentation, *Philos. Mag.* 85 (2005) 2177–2195, <https://doi.org/10.1080/14786430412331331862>.
- [42] X. Li, D.L. Irving, L. Vitos, First-principles investigation of the micromechanical properties of fcc-hcp polymorphic high-entropy alloys, *Sci. Rep.* 8 (2018) 4–11, <https://doi.org/10.1038/s41598-018-29588-z>.
- [43] D.F. Bahr, D.E. Kramer, W.W. Gerberich, Non-linear deformation mechanisms during nanoindentation, *Acta Mater.* 46 (1998) 3605–3617, [https://doi.org/10.1016/S1359-6454\(98\)00024-X](https://doi.org/10.1016/S1359-6454(98)00024-X).
- [44] S. Lee, A. Vaid, J. Im, B. Kim, A. Prakash, J. Guénolé, D. Kiener, E. Bitzek, S.H. Oh, In-situ observation of the initiation of plasticity by nucleation of prismatic dislocation loops, *Nat. Commun.* 11 (2020) 1–11, <https://doi.org/10.1038/s41467-020-15775-y>.
- [45] T.H. Ahn, C.S. Oh, D.H. Kim, K.H. Oh, H. Bei, E.P. George, H.N. Han, Investigation of strain-induced martensitic transformation in metastable austenite using nanoindentation, *Scr. Mater.* 63 (2010) 540–543, <https://doi.org/10.1016/j.scriptamat.2010.05.024>.
- [46] T.H. Ahn, S.B. Lee, K.T. Park, K.H. Oh, H.N. Han, Strain-induced  $\epsilon$ -martensite transformation during nanoindentation of high-nitrogen steel, *Mater. Sci. Eng. A* 598 (2014) 56–61, <https://doi.org/10.1016/j.msea.2014.01.030>.
- [47] A. Gouldstone, N. Chollacoop, M. Dao, J. Li, A.M. Minor, Y.L. Shen, Indentation across size scales and disciplines: Recent developments in experimentation and modeling, *Acta Mater.* 55 (2007) 4015–4039, <https://doi.org/10.1016/j.actamat.2006.08.044>.
- [48] C.A. Klein, G.F. Cardinale, Young's modulus and Poisson's ratio of CVD diamond, *Diam. Relat. Mater.* 2 (1993) 918–923, [https://doi.org/10.1016/0925-9635\(93\)90250-6](https://doi.org/10.1016/0925-9635(93)90250-6).
- [49] T. Chen, L. Tan, Z. Lu, H. Xu, The effect of grain orientation on nanoindentation behavior of model austenitic alloy Fe-20Cr-25Ni, *Acta Mater.* 138 (2017) 83–91, <https://doi.org/10.1016/j.actamat.2017.07.028>.
- [50] J.R. Cahoon, W.H. Broughton, A.R. Kutzak, The determination of yield strength from hardness measurements, *Metall. Trans. 2* (1971) 1979–1983, <https://doi.org/10.1007/BF02913433>.
- [51] C.A. Schuh, Nanoindentation studies of materials, *Mater. Today*. 9 (2006) 32–40, [https://doi.org/10.1016/S1369-7021\(06\)71495-X](https://doi.org/10.1016/S1369-7021(06)71495-X).
- [52] J.M. Moyer, G.S. Ansell, The volume expansion accompanying the martensite transformation in iron-carbon alloys, *Metall. Trans. A* 6 (1975) 1785–1791, <https://doi.org/10.1007/BF02642308>.
- [53] J.E. Bradby, J.S. Williams, M.V. Swain, Pop-in events induced by spherical indentation in compound semiconductors, *J. Mater. Res.* 19 (2004) 380–386, <https://doi.org/10.1557/jmr.2004.19.1.380>.
- [54] S. Sinha, S.S. Nene, M. Frank, K. Liu, P. Agrawal, R.S. Mishra, On the evolving nature of  $c/a$  ratio in a hexagonal close-packed epsilon martensite phase in transformative high entropy alloys, *Sci. Rep.* 9 (2019) 1–14, <https://doi.org/10.1038/s41598-019-49904-5>.
- [55] Y.F. Guo, S. Xu, X.Z. Tang, Y.S. Wang, S. Yip, Twinnability of hcp metals at the nanoscale, *J. Appl. Phys.* 115 (2014), <https://doi.org/10.1063/1.4881756>.
- [56] J.H. Shin, S.H. Kim, T.K. Ha, K.H. Oh, I.S. Choi, H.N. Han, Nanoindentation study for deformation twinning of magnesium single crystal, *Scr. Mater.* 68 (2013) 483–486, <https://doi.org/10.1016/j.scriptamat.2012.11.030>.
- [57] Y.T. Cheng, C.M. Cheng, Scaling approach to conical indentation in elastic-plastic solids with work hardening, *J. Appl. Phys.* 84 (1998) 1284–1291, <https://doi.org/10.1063/1.368196>.
- [58] X. He, D. Cai, Y. Shao, H. Bao, J. Han, Laplacian regularized Gaussian mixture model for data clustering, *IEEE Trans. Knowl. Data Eng.* 23 (2011) 1406–1418, <https://doi.org/10.1109/TKDE.2010.259>.